Nano Research

Open Access

Research Article

A robust anti-thermal quenching red phosphors: $Cs_2ZrCl_6:Sb^{3+}$

Haoyi Zhang[§], Jingtao Jia[§], Baowei Zhang ✉, and Siyu Lu ✉

College of Chemistry, Zhengzhou University, Zhengzhou 450001, China
[§] Haoyi Zhang and Jingtao Jia contributed equally to this work.

Cite this article: *Nano Research*, **2026**, *19*, 94908432. https://doi.org/10.26599/NR.2026.94908432

ABSTRACT: Most of phosphors undergo thermal quenching (TQ) at high temperature, due to thermal-activated non-radiative transitions. TQ effects lead to significant reduced luminous efficiency of phosphors at high operation temperature, hindering their application in high power phosphor-converted white light-emitting diodes (WLED). Here, we report a zero-dimensional metal halide perovskite: $Cs_2ZrCl_6:Sb^{3+}$, exhibiting robust anti-TQ red emission up to 500 K, comparable to the mainstream anti-TQ phosphors (e.g. $K_2SiF_6:Mn^{4+}$). The hetero-valent doping of Sb^{3+} induces structure defects of host and thus compensate the non-radiative emission loss through thermal accelerated energy transfer from defects to emitter at high temperature. We assembled the red anti-TQ phosphor into a white light-emitting diode (WLED) device, achieving stable output light intensity and chromaticity up to 2000 mA.

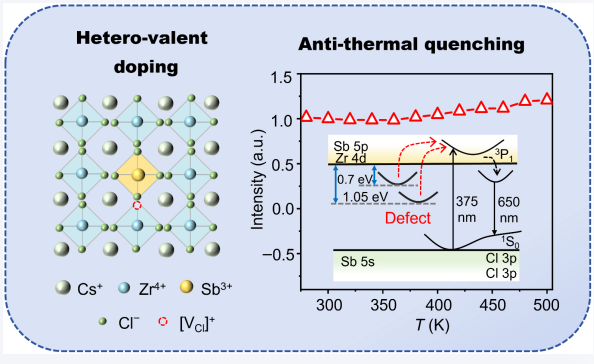

KEYWORDS: anti-thermal quenching, metal halide perovskite, hetero-valent doping, high power white light-emitting diode (WLED)

1 Introduction

Higher power phosphor-converted white light-emitting diodes (WLEDs) are the best energy-saving devices for outdoor lighting that occupies > 40% of electricity consumption in urban society [1]. However, high-power elevates operation temperatures of WLEDs to 200 °C [2], triggering thermal quenching (TQ) of phosphors through thermal activated non-radiative transition [3]. To preserve the luminescence intensity and chromaticity of WLEDs, the anti-TQ phosphors are required [4, 5].

The mainstream anti-TQ phosphors are metal oxides/nitrides [6, 7]. For example, Li et al. [8] reported that the $Y_3Sc_2Al_3O_{12}$:5% Cr^{3+} sample exhibited high photoluminescence quantum yield (PLQY = 74%) and near-zero TQ up to 423 K. Its high structural rigidity avoids significant thermal-expansion of lattice, preserving the structure of emission center at high temperature. Bai et al. [9] prepared a red phosphor: $K_2MgGeO_4:Eu^{3+}$, offering high PLQY (94.98%) and near-zero TQ up to 573 K. These metal oxides/nitrides are usually synthesized at high temperature (> 1000 °C) [5, 6, 8–11].

Received: November 16, 2025; **Revised:** December 30, 2025
Accepted: January 12, 2026

✉Address correspondence to Baowei Zhang, baoweizhang@zzu.edu.cn; Siyu Lu, sylu2013@zzu.edu.cn

Recently, series of metal halides have been developed as anti-TQ phosphors [12–17], which are synthesized at lower temperature or even at room temperature [12, 18–20]. For example, Han et al. [12] observed zero-TQ behavior in $Rb_3(Cd_{0.80}Mn_{0.20})_2Cl_7$ single crystals, preserving 100% photoluminescence (PL) intensity of room temperature at 423 K. This TQ performance mainly attributed to the supply of additional charge carriers from traps to Mn^{2+} luminescent centers at high temperature. Zhou et al. [13] reported that $CsCdCl_3:Mn^{2+}$, Zr^{4+} powders displayed zero-TQ radioluminescence up to 448 K under the excitation of X-ray. Zhang et al. [14] reported Sb^{3+} doped Rb_3InCl_6 featuring robust anti-TQ behavior up to 500 K, thanks to the intrinsic structure rigidity of isolated octahedra in zero-dimensional (0D) framework. These results indicate, after proper structure design, metal halides can approach to robust anti-TQ properties, comparable to the commercial anti-TQ phosphors [12–14, 16, 17].

Here, we report a non-toxic, red anti-TQ phosphor: $Cs_2ZrCl_6:x Sb^{3+}$, which was synthesized via a simple co-precipitation method [18]. This material, firstly developed by Chen et al. [18], exhibiting dual luminescence originating from intrinsic host self-trapped exciton (STE) and Sb^{3+} induced extrinsic STE, show promising application potential on anti-counterfeiting [21] and WLED devices [22]. Under 375 nm excitation, this material exhibits STE emission at 650 nm, with a PLQY of 30% (Fig. S1 in the Electronic Supplementary Material (ESM)). More importantly, this

red emission preserves 120% PL intensity of room temperature at 500 K, exhibiting robust anti-TQ properties. Thermoluminescence (TL) revealed a broad energy distribution of defects ranging from 0.7 to 1.05 eV [12]. At high temperature, the energy transfer from the defects to dopants is accelerated, compensating the non-radiative loss and thus achieving anti-TQ emission. To verify this hypothesis, the homo-valent doped Cs_2ZrCl_6:xTe^{4+} was also prepared as a control sample. This sample only forms shallow defects (0.7 eV) and its emission quenches straightly from room temperature to 360 K, supporting the relation between the hetero (or homo)-valent doping, defect depth, and anti-TQ properties. we further incorporated the Cs_2ZrCl_6:xSb^{3+}, combining with the ultraviolet (UV) light-emitting diode (LED) chip and another green anti-TQ phosphor (Rb_3InCl_6:xSb^{3+}) [14], into the high-power WLED. This device emits stable light intensity and chromaticity up to 2000 mA, overpassing the red emission carbon dots [23] and commercial red phosphors (e.g. $CaAlSiN_3$:Eu^{2+}) and almost as good as mainstream anti-TQ red phosphors (e.g. K_2SiF_6:Mn^{4+}).

2 Results and discussion

The polycrystalline powders of Cs_2ZrCl_6:xSb^{3+}, and Cs_2ZrCl_6:xTe^{4+} were all prepared using the coprecipitation method [18]. Taking Cs_2ZrCl_6:xSb^{3+} as an example: 2 mmol CsCl was dissolved in 0.5 mL HCl aqueous (37%) as a stock solution. x mmol $SbCl_3$ and 1–x mmol $ZrCl_4$ were dissolved into 5 mL HCl aqueous (37%). The x is in the range of 0–0.1 mmol. This mixture was heated to 110 °C, and then the CsCl stock solution was poured. A white precipitate formed immediately and the reaction proceeded for 3 min. The reaction solution was then centrifuged at 6000 r/min for 3 min and the collected precipitation was rinsed three times by excess isopropanol to remove residual HCl. Finally, this precipitation was dried in a vacuum oven at 60 °C for 10 h. The synthesis of Cs_2ZrCl_6:xTe^{4+} is similar to that of Cs_2ZrCl_6:Sb^{3+}, except replacing $SbCl_3$ by $TeCl_4$.

The XRD patterns confirmed a pure phase of Cs_2ZrCl_6:xSb^{3+} (x: 0%–4.6%) samples, matching well with the cif of Cs_2ZrCl_6 (ICSD No. 26695). The main peak at ~24° shifted toward smaller angles with increasing doping concentration, due to the larger ionic radius of Sb^{3+} compared to Zr^{4+} (Fig. 1(a)). Concurrently, inductively coupled plasma-optical emission spectrometer (ICP-OES) confirmed that the actual Sb^{3+} doping concentration was in the range of 0.5%–4.6% (Table S1 in the ESM). Temperature-dependent PL spectra of Cs_2ZrCl_6:3.3% Sb^{3+} sample was collected at temperature range from 280 to 500 K (Fig. 1(b)). The emission peak position shifted little and the luminescence intensity slightly enhanced when the temperature increased from 280 to 500 K. In details, the PL intensity reached a maximum at 500 K, approximately 120% of the PL intensity at 300 K, exhibiting robust anti-TQ properties (Fig. 1(c)). Subsequently, multiple heating-cooling cycles from 300 to 500 K were performed on the Cs_2ZrCl_6:3.3% Sb^{3+} sample to verify the stability and reproducibility (Fig. 1(d) and Fig. S2 in the ESM). After ten cycles, no significant loss in PL intensity was observed. Continuous 15 h PL measurements conducted at 460, 480, and 500 K revealed no decay in PL intensity under sustained high temperatures, confirming strong thermal stability (Fig. S3 in the ESM). Subsequently, the XRD patterns of Cs_2ZrCl_6:3.3% Sb^{3+} were collected during heating-cooling cycles from 298 to 523 K (Fig. 1(e) and Fig. S4 in the ESM). The diffraction peaks initially shifted toward small angles as temperature increased, attributing to lattice expansion. After cooling, the peaks shifted toward large angles, and finally returned back to their original positions without the emergence of any impurity peaks. These experiments demonstrate the robust anti-TQ and structural stability of Cs_2ZrCl_6:3.3% Sb^{3+} phosphors.

The other dopant concentrations of Sb^{3+} were also synthesized and their temperature-dependent PL intensity were plotted, as shown in Fig. 2(a) and Fig. S5 in the ESM. It was evidenced that 2.1%–3.3% was the optimal doping concentration to achieve anti-TQ property. Thermoluminescence (TL) was employed (Fig. 2(b))

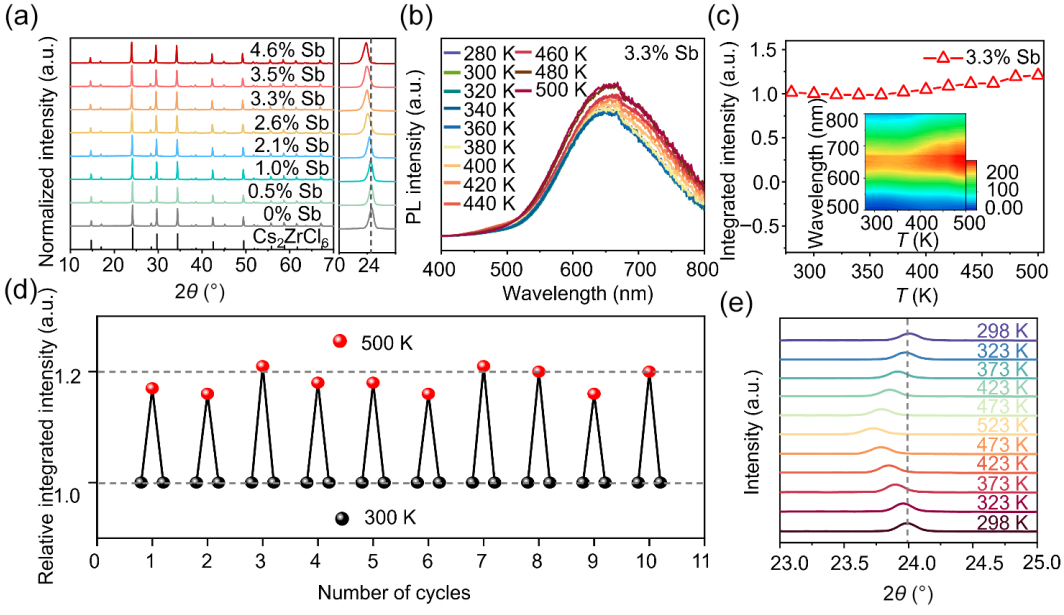

Figure 1 (a) Powder XRD patterns of Cs_2ZrCl_6:xSb^{3+} (x = 0.5%, 1.0%, 2.1%, 2.6%, 3.3%, 3.5%, 4.6%). The peak shift at 24° is shown in the enlarged window. The standard XRD patterns of Cs_2ZrCl_6 (ICSD No. 26695) are also provided for reference. (b) Temperature-dependent (280–500 K) PL spectra of Cs_2ZrCl_6:xSb^{3+} excited by 375 nm. (c) Normalized temperature-dependent PL of Cs_2ZrCl_6:xSb^{3+} (normalized by the PL intensity at 300 K as 1). (d) Ten heating–cooling cycles for Cs_2ZrCl_6:xSb^{3+} from 300 to 500 K. The PL intensity (normalized by the PL intensity at 300 K as 1) is recorded at 300 K (black dots) and 500 K (red dots), respectively. (e) Temperature-dependent XRD patterns of Cs_2ZrCl_6:xSb^{3+} from 298 to 523 K in one heating–cooling cycle.

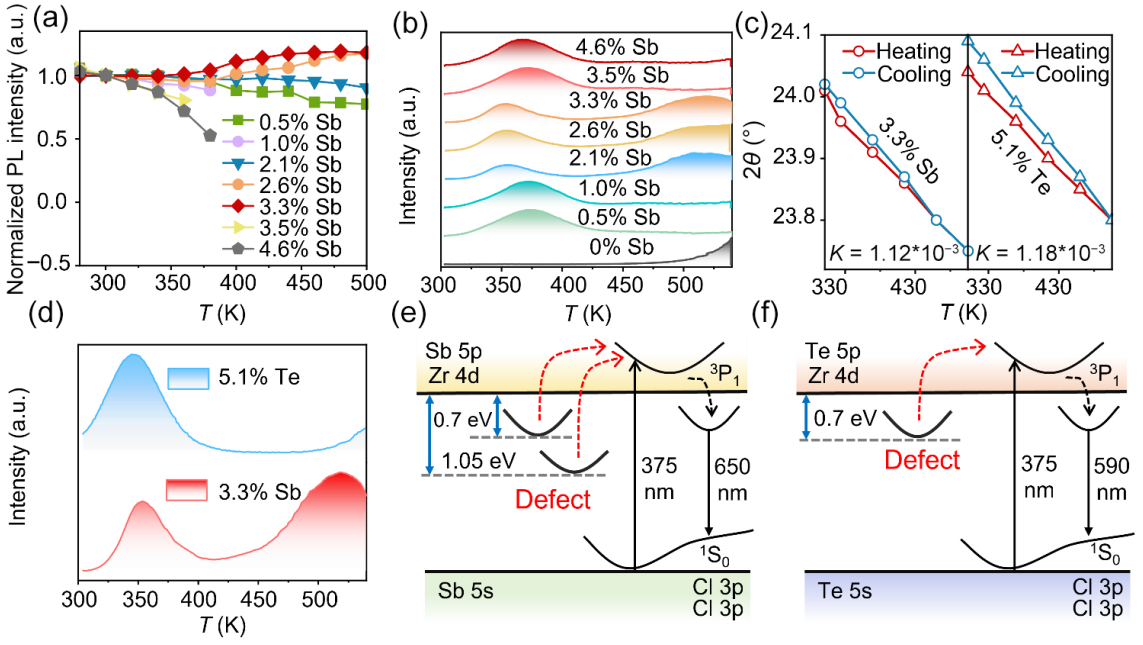

Figure 2 (a) Temperature-dependent PL intensity of Cs_2ZrCl_6:3.3% Sb^{3+} from 280 to 500 K, with x ranging from 0.5% to 4.6%, and PL intensity normalized by the PL intensity at 300 K as 1. (b) Thermoluminescence spectra of Cs_2ZrCl_6:$x$$Sb^{3+}$ with different doping concentrations (x = 0.5%–4.6%). (c) Position of XRD peaks for Cs_2ZrCl_6:3.3% Sb^{3+} and Cs_2ZrCl_6:5.1% Te^{4+} in one heating–cooling cycle from 298 to 523 K and their fitted slope. (d) Thermoluminescence spectra of Cs_2ZrCl_6:3.3% Sb^{3+} and Cs_2ZrCl_6:5.1% Te^{4+}. (e) Diagram of emission process of Cs_2ZrCl_6:3.3% Sb^{3+} under 375 nm excitation and the energy compensation process. (f) Diagram of emission process of Cs_2ZrCl_6:5.1%Te^{4+} under 375 nm excitation and the energy compensation process.

to reveal the energy distribution of defects by thermal-induced luminescence. The undoped Cs_2ZrCl_6 (0% Sb^{3+}) does not show significant defects emission in the temperature from 300 to 540 K. In contrast, 0.5%–1.0% doping concentration of Sb^{3+} results in a TL peak at ~375 K, indicating a trap depth (E_a) of defects as 0.75 eV (E_a = T(K)/500) [12]. As the increase of dopant concentration (2.1%–3.3% Sb^{3+}), a deeper trap was formed with an E_a = 1.05 eV, accompany with the beginning shallow traps (E_a = 0.70 eV). Such broad energy distribution of defects could compensate the non-radiative emission loss at each heating stage and realize zero-thermal quenching from 300 to 500 K, through thermal accelerated energy transfer. To further verify this hypothesis, Cs_2ZrCl_6:Te^{4+} was prepared as control sample. This homo-valent doped sample shared the same host with Cs_2ZrCl_6:Sb^{3+}, but did not exhibit anti-TQ at high temperature. The temperature-dependent XRD patterns of Cs_2ZrCl_6:Te^{4+} were collected (Fig. S6 in the ESM). As shown in Fig. 2(c), the temperature-dependent diffraction peak shifts of Cs_2ZrCl_6:5.1%Te^{4+} and Cs_2ZrCl_6:3.3% Sb^{3+} were plotted, to evaluate the lattice-expansion in one cycle of heating–cooling from 300 to 525 to 300 K. Both the peaks of Cs_2ZrCl_6:3.3% Sb^{3+} and Cs_2ZrCl_6:5.1% Te^{4+} shifted to small-angles (lattice expansion) at heating and large-angles (lattice contraction) at cooling, and the fitted slope was $-1.12\times10^3\times2\theta$ K^{-1} for Cs_2ZrCl_6:Sb^{3+} and $-1.18\times10^3\times2\theta$ K^{-1} for Cs_2ZrCl_6:Te^{4+} respectively. This slight difference on this thermal lattice expansion behavior indicated these two samples had similar structure rigidity and the difference of their anti-TQ properties should attribute to other reasons. Subsequently, the TL spectra of Cs_2ZrCl_6:5.1% Te^{4+} only show shallow traps (Fig. 2(d)), while the Cs_2ZrCl_6:3.3% Sb^{3+} exhibits broader and deeper traps. The shallow traps are not enough to compensate the emission loss through energy transfer at the temperature beyond 350 K (the peak of TL spectra). In contrast, the hetero-valent doping of Sb^{3+} triggers deep and broad energy distribution of defects in the lattice and thus results in robust anti-TQ property.

Based on the above experimental data, we have drawn the energy transfer mechanism diagrams for Cs_2ZrCl_6:Sb^{3+} and Cs_2ZrCl_6:Te^{4+} (Figs. 2(e) and 2(f)). For Cs_2ZrCl_6:Sb^{3+}, upon 375 nm excitation, Sb^{3+} ions are excited from the ground state ($^1S_0$) to the excited state ($^3P_1$), which induces self-trapped exciton emissions with broadband red luminescence at 650 nm ($^3P_1$→$^1S_0$). However, some excitons will experience non-radiative processes. As the temperature rises, non-radiative processes will be accelerated, this will result in emission loss of the phosphor. Due to Sb's hetero-valent doping, two broad and deep traps are generated at high temperatures. The depths of the two defects are 0.70 and 1.05 eV respectively, calculated via the above TL spectra, which are sufficient to compensate for thermal emission losses. Similarly, Cs_2ZrCl_6:Te^{4+} under 375 nm excitation emits yellow luminescence at 590 nm ($^3P_1$→$^1S_0$). However, the homo-valent doping only induces shallow traps, with an energy depth of 0.70 eV. This shallow defect is not enough to compensate for the radiation loss in a wide high temperature window.

We evaluated the practical feasibility of Cs_2ZrCl_6:$x$$Sb^{3+}$ phosphor by fabricating high-power white LEDs using a LED chip (λ_{max} = 380 nm) as the light source and another anti-TQ phosphor Rb_3InCl_6:$x$$Sb^{3+}$ as the green-light source. Commercial red phosphor $CaAlSiN_3$:Eu^{2+} (emission peak at 645 nm), red emission carbon dots, and mainstream anti-TQ phosphor K_2SiF_6:Mn^{4+} were employed as control samples. Firstly, Cs_2ZrCl_6:$x$$Sb^{3+}$, $CaAlSiN_3$:Eu^{2+}, carbon dots, and K_2SiF_6:Mn^{4+} were individually coated onto the surface of the UV LED chip. As shown in Fig. 3(a), the EL intensity of Cs_2ZrCl_6:xSb^{3+} continued to increase steadily flowing the increase of current. K_2SiF_6:Mn^{4+} exhibited robust stability and only slightly declined at 1200 mA. When the current exceeded 1200 mA, $CaAlSiN_3$:Eu^{2+} exhibited obvious TQ. Although the electroluminescence (EL) intensity of the carbon dots shows an upward trend with increasing current, it remains unstable.

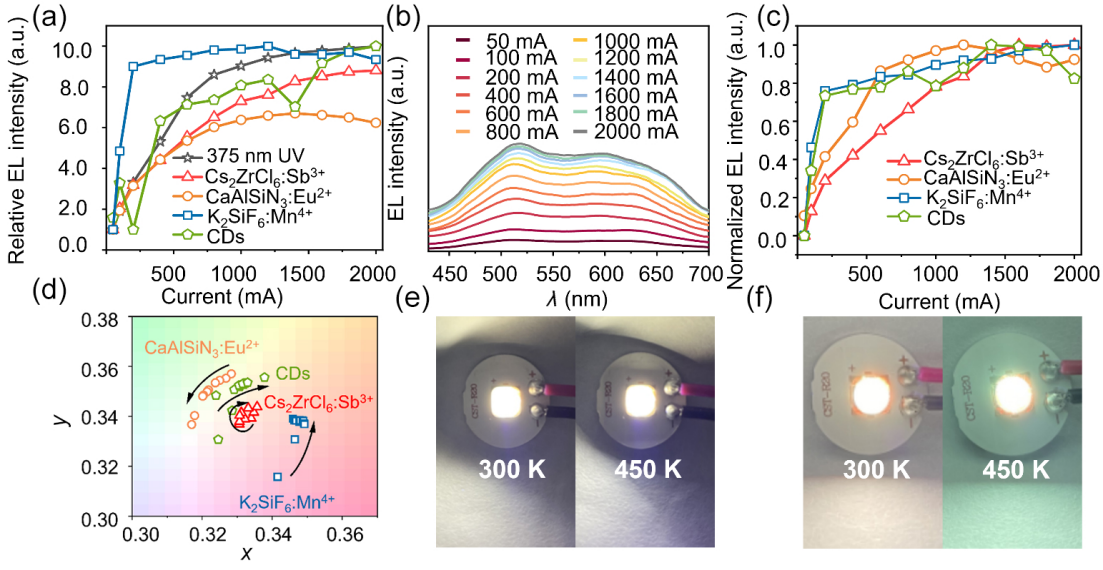

Figure 3 Performance of WLEDs at high operating currents. (a) EL spectra of $Cs_2ZrCl_6:xSb^{3+}$ (red line and triangle), commercial red phosphor $CaAlSiN_3:Eu^{2+}$ (orange line and circle), commercial anti-thermal quenching phosphor $K_2SiF_6:Mn^{4+}$ (blue line and square) and carbon dots (green line and pentagon) coated on UV LED chips under high-flux operating currents of 50–2000 mA. EL intensity from UV-LED chip was also recorded for reference (grey line and star). (b) EL spectra of WLEDs using $Cs_2ZrCl_6:xSb^{3+}$ as the red phosphor and $Rb_3InCl_6:xSb^{3+}$ as the green phosphor within the current range of 50–2000 mA. (c) Normalized electroluminescence intensity spectra of WLEDs using $Cs_2ZrCl_6:xSb^{3+}$ (red line and triangle), commercial red phosphor $CaAlSiN_3:Eu^{2+}$ (orange line and circle), commercial anti-thermal quenching phosphor $K_2SiF_6:Mn^{4+}$ (blue line and square) and carbon dots (green line and pentagon) respectively as the red phosphor and $Rb_3InCl_6:xSb^{3+}$ as the green phosphor within the current range of 50–2000 mA. (d) CIE coordinates based on $Cs_2ZrCl_6:xSb^{3+}$ (triangle) compared with commercial red phosphors $CaAlSiN_3:Eu^{2+}$ (circle), commercial anti-thermal quenching phosphor $K_2SiF_6:Mn^{4+}$ (square), and carbon dots (pentagon). (e) Photographs of WLEDs using $Cs_2ZrCl_6:xSb^{3+}$ and (f) commercial red phosphor $CaAlSiN_3:Eu^{2+}$ at low current (300 K, left) and high current (450 K, right), respectively.

Subsequently, we integrated $Cs_2ZrCl_6:xSb^{3+}$, $CaAlSiN_3:Eu^{2+}$, carbon dots, and $K_2SiF_6:Mn^{4+}$ respectively with the UV LED chip and the green anti-TQ phosphor ($Rb_3InCl_6:xSb^{3+}$). The $Cs_2ZrCl_6:xSb^{3+}$-based WLED maintained enhanced luminous intensity with the increased current up to 2000 mA (Figs. 3(b) and 3(c)), corresponding to an operating temperature of approximately 450 K (taken by thermal-vision-camara, Fig. S7 in the ESM). The $Cs_2ZrCl_6:xSb^{3+}$-based WLED maintained stable white color across 50–2000 mA (Fig. 3(d)). The electroluminescence intensity of $K_2SiF_6:Mn^{4+}$-based WLED increased as the current steadily increased (Fig. 3(c) and Fig. S8 in the ESM). Also, the chromatic coordinate of the $K_2SiF_6:Mn^{4+}$-based WLED gradually stabilized as the current increased (Fig. 3(d)). The electroluminescence intensity of carbon dots-based WLED increased as the current intensity increased initially; however, when the current reached 1400 mA, the electroluminescence intensity began to decrease (Fig. 3(c) and Fig. S9 in the ESM). As a result, the chromatic coordinate of carbon dots-based WLED shifted toward yellow at high applied current (Fig. 3(d)). The overall luminous intensity of the $CaAlSiN_3:Eu^{2+}$-based WLED began to decay when the applied current was over 1200 mA (Fig. 3(c) and Fig. S10 in the ESM). As shown in Fig. 3(d), The $CaAlSiN_3:Eu^{2+}$-based WLED exhibited color transitioning from white to green, attributing to the TQ of $CaAlSiN_3:Eu^{2+}$. The performance of the WLED at 200 and 2000 mA is shown in Fig. 3(e) ($Cs_2ZrCl_6:xSb^{3+}$-based) and 3(f) ($CaAlSiN_3:Eu^{2+}$-based), respectively. The fabricated $Cs_2ZrCl_6:xSb^{3+}$-based WLEDs exhibited stable, bright white light under high-current conditions (Fig. 3(e)), while the white light of $CaAlSiN_3:Eu^{2+}$-based one deteriorated to green (Fig. 3(f)). Carbon dots-based WLED and $K_2SiF_6:Mn^{4+}$-based WLED photographs at low and high current operating conditions are shown in Figs. S8 and S9 in the ESM. In general, the $Cs_2ZrCl_6:xSb^{3+}$-WLED overpass the red-emission carbon dots and commercial red phosphors (e.g., $CaAlSiN_3:Eu^{2+}$) and almost as good as mainstream anti-TQ red phosphors (e.g., $K_2SiF_6:Mn^{4+}$). Meanwhile, aging tests confirmed the $Cs_2ZrCl_6:xSb^{3+}$-based WLED device's long-term stability under humid and high-current conditions (Figs. S11 and S12 in the ESM). Therefore, $Cs_2ZrCl_6:xSb^{3+}$ phosphors are thermally stable and are suitable for application as a red phosphor in high-power WLED illumination.

3 Conclusions

This study synthesized $Cs_2ZrCl_6:xSb^{3+}$ phosphors exhibiting robust anti-TQ behavior, maintaining 120% of their room-temperature (300 K) fluorescence intensity at 500 K. The hetero-valent doping induces high concentration of defects in host lattice. Through thermal-activated energy transfer from defects to emitter, the non-radiative emission loss is compensated, thus realizing robust anti-TQ. High power WLED devices were fabricated employing anti-TQ metal halides as red ($Cs_2ZrCl_6:xSb^{3+}$) and green ($Rb_3InCl_6:xSb^{3+}$) light-emitting components, maintaining stable intensity and chromaticity even at operating currents as high as 2000 mA. We hope this work would further stimulate the discovery and extension of new anti-TQ metal halide phosphors.

Electronic Supplementary Material: Supplementary material (including details of characterizations of the sample) is available in the online version of this article at https://doi.org/10.26599/NR.2026.94908432.

Data availability

All data needed to support the conclusions in the paper are presented in the manuscript and/or the Electronic Supplementary

Material. Additional data related to this paper may be requested from the corresponding author upon request.

Acknowledgements

This work was supported by the National Natural Science Foundation of China (Nos. 22305224 and U24A2079), the China Postdoctoral Science Foundation (No. 2022TQ0290), and the Ministry of Science and Technology of China (No. DL2023026004L). The Center of Advanced Analysis & Gene Sequencing, Zhengzhou University was also gratefully acknowledged.

Declaration of competing interest

All the contributing authors report no conflict of interests in this work.

Author contribution statement

H. Y. Z.: writing manuscript, validation, data curation. J. T. J.: investigation, characterization, data analysis. B. W. Z. and S. Y. L.: conceptualization, project administration, funding acquisition, supervision, writing and editing the final draft. All the authors have approved the final manuscript.

Use of AI statement

None.

References

[1] Ożadowicz, A.; Grela, J. Energy saving in the street lighting control system—a new approach based on the EN-15232 standard. *Energy Effic.* **2017**, *10*, 563–576.

[2] Kim, Y. H.; Arunkumar, P.; Kim, B. Y.; Unithrattil, S.; Kim, E.; Moon, S. H.; Hyun, J. Y.; Kim, K. H.; Lee, D.; Lee, J. S. et al. A zero-thermal-quenching phosphor. *Nat. Mater.* **2017**, *16*, 543–550.

[3] Amachraa, M.; Wang, Z. B.; Chen, C.; Hariyani, S.; Tang, H. M.; Brgoch, J.; Ong, S. P. Predicting thermal quenching in inorganic phosphors. *Chem. Mater.* **2020**, *32*, 6256–6265.

[4] Guo, F.; Yuan, R.; Yang, Y. L.; Zhao, J. T.; Lin, H.; Zhang, Z. J. An effective heat dissipation strategy improving efficiency and thermal stability of phosphor-in-glass for high-power WLEDs. *Ceram. Int.* **2022**, *48*, 13185–13192.

[5] Lin, C. C.; Tsai, Y. T.; Johnston, H. E.; Fang, M. H.; Yu, F. J.; Zhou, W. Z.; Whitfield, P.; Li, Y.; Wang, J.; Liu, R. S. et al. Enhanced photoluminescence emission and thermal stability from introduced cation disorder in phosphors. *J. Am. Chem. Soc.y* **2017**, *139*, 11766–11770.

[6] Qiao, J. W.; Ning, L. X.; Molokeev, M. S.; Chuang, Y. C.; Liu, Q. L.; Xia, Z. G. Eu^{2+} site preferences in the mixed cation $K_2BaCa(PO_4)_2$ and thermally stable luminescence. *J. Am. Chem. Soc.* **2018**, *140*, 9730–9736.

[7] Wang, L.; Xie, R. J.; Suehiro, T.; Takeda, T.; Hirosaki, N. Down-conversion nitride materials for solid state lighting: Recent advances and perspectives. *Chem. Rev.* **2018**, *118*, 1951–2009.

[8] Li, H.; Jiao, J. K.; Xiang, X. F.; Wu, J. Z.; Hu, W. B.; Xie, J. Y.; Huang, S. P.; Zhang, H. Z.; Zhu, J. Directly identifying multiple Cr^{3+} emitting centers for broad near-infrared emission in an efficient and near-zero thermal quenching garnet-type phosphor. *Adv. Opt. Mater.* **2024**, *12*, 2302391.

[9] Bai, Y. X.; Jia, Z. W.; Gao, J. Y.; Wu, L.; Kong, Y. F.; Zhang, Y.; Xu, J. J. A novel red-emitting phosphor $K_2MgGeO_4:Eu^{3+}$ for WLEDs: Zero-thermal quenching induced by heterovalent substitution. *J. Mater. Chem. C* **2022**, *10*, 15957–15966.

[10] Cui, D. P.; Song, Z.; Xia, Z. G.; Liu, Q. L. Luminescence tuning, thermal quenching, and electronic structure of narrow-band red-emitting nitride phosphors. *Inorg. Chem.* **2017**, *56*, 11837–11844.

[11] Yang, Z. Y.; de Boer, T.; Braun, P. M.; Su, B. B.; Zhang, Q. Y.; Moewes, A.; Xia, Z. G. Thermally stable red-emitting oxide ceramics for laser lighting. *Adv. Mater.* **2023**, *35*, 2301837.

[12] Han, J. H.; Viswanath, N. S. M.; Park, Y. M.; Cho, H. B.; Jang, S. W.; Min, J. W.; Im, W. B. Zero-thermal-quenching layered metal halide perovskite. *Chem. Mater.* **2022**, *34*, 5690–5697.

[13] Zhou, X. Q.; Han, K.; Wang, Y. X.; Jin, J. C.; Jiang, S. D.; Zhang, Q. Y.; Xia, Z. G. Energy-trapping management in X-ray storage phosphors for flexible 3D imaging. *Adv. Mater.* **2023**, *35*, 2212022.

[14] Zhang, B. W.; Ru, Y.; Zhou, J. Q.; Jia, J. T.; Song, H. Q.; Liu, Z. Y.; Zhang, L. L.; Liu, X. Y.; Zhong, G. M.; Yong, X. et al. A robust anti-thermal-quenching phosphor based on zero-dimensional metal halide $Rb_3InCl_6:xSb^{3+}$. *J. Am. Chem. Soc.* **2024**, *146*, 7658–7667.

[15] Liu, S. Y.; Fang, X. Y.; Lu, B.; Yan, D. P. Wide range zero-thermal-quenching ultralong phosphorescence from zero-dimensional metal halide hybrids. *Nat. Commun.* **2020**, *11*, 4649.

[16] Tang, Z.; Liu, R. Z.; Chen, J. S.; Zheng, D. Y.; Zhou, P. W.; Liu, S. P.; Bai, T. X.; Zheng, K. B.; Han, K. L.; Yang, B. Highly efficient and ultralong afterglow emission with anti-thermal quenching from $CsCdCl_3$:Mn perovskite single crystals. *Angew. Chem., Int. Ed.* **2022**, *61*, e202210975.

[17] Liu, M. M.; Wan, Q.; Wang, H. M.; Carulli, F.; Sun, X. C.; Zheng, W. L.; Kong, L.; Zhang, Q.; Zhang, C. Y.; Zhang, Q. G. et al. Suppression of temperature quenching in perovskite nanocrystals for efficient and thermally stable light-emitting diodes. *Nat. Photonics* **2021**, *15*, 379–385.

[18] Chen, B.; Guo, Y.; Wang, Y.; Liu, Z.; Wei, Q.; Wang, S. X.; Rogach, A. L.; Xing, G. C.; Shi, P.; Wang, F. Multiexcitonic emission in zero-dimensional $Cs_2ZrCl_6:Sb^{3+}$ perovskite crystals. *J. Am. Chem. Soc.* **2021**, *143*, 17599–17606.

[19] Mandal, S.; Roy, D.; De, C. K.; Ghosh, S.; Mandal, M.; Das, A.; Mandal, P. K. Instantaneous, room-temperature, open-air atmosphere, solution-phase synthesis of perovskite quantum dots through halide exchange employing non-metal based inexpensive HCl/HI: Ensemble and single particle spectroscopy. *Nanoscale Adv.* **2019**, *1*, 3506–3513.

[20] Zhao, C. L.; Gao, Y.; Qiu, J. B. Achieving multicolor emitting of antimony-doped indium-based halide perovskite via monovalent metal induced phase engineering. *ACS Appl. Mater. Interfaces* **2023**, *15*, 59610–59617.

[21] Chen, Q. C.; Ma, X. H.; Dong, G. F.; Yan, H. B. Mechanochemical synthesis of Sb^{3+}-doped Cs_2ZrCl_6 double perovskites for excitation-wavelength-responsive trimodal luminescence and high-level anti-counterfeiting. *RSC Adv.* **2025**, *15*, 26800–26806.

[22] Chen, C. H.; Xiang, J. M.; Chen, Y. H.; Jin, M. K.; Zheng, J. M.; Zhang, N. M.; Guo, C. F. White-light emission lead-free perovskite phosphor $Cs_2ZrCl_6:Sb^{3+}$. *Ceram. Int.* **2022**, *48*, 1851–1856.

[23] Zhang, Y. Q.; Ding, S. R.; Yu, J. K.; Sui, L. Z.; Song, H. Q.; Hu, Y. S.; Waterhouse, G. I. N.; Tang, Z. Y.; Lu, S. Y. Unveiling the photoluminescence mechanisms of carbon dots through tunable near-infrared dual-wavelength lasing. *Matter* **2024**, *7*, 3518–3536.